



## Assessment of variation of land use/land cover and its impact on land surface temperature of Asansol subdivision

Niladri Das <sup>a,\*</sup>, Prolay Mondal <sup>b</sup>, Subhasish Sutradhar <sup>b</sup>, Ranajit Ghosh <sup>c</sup>



<sup>a</sup> Department of Geography, Hiralal Bhakat College, Nalhati, Birbhum, West Bengal 731220, India

<sup>b</sup> Department of Geography, Raiganj University, Raiganj, Uttar Dinajpur, 733134, India

<sup>c</sup> Department of Geography, Suri Vidyasagar College, Suri, Birbhum, West Bengal 731101, India

### ARTICLE INFO

#### Article history:

Received 30 January 2020

Revised 6 April 2020

Accepted 3 May 2020

Available online xxxx

#### Keywords:

Simulation

Normalized difference vegetation index (NDVI)

Land use and land cover (LULC)

Normalized difference build-up index (NDBI)

Normalized difference water index (NDWI)

Land surface temperature (LST)

### ABSTRACT

Economic development is a basic need for the growth of the region and it stimulates the rapid transformation of land use and land cover (LULC) units. Urbanization and industrialization are one of the major factors to increase temperature. Asansol sub-division is one of the important industrial and urbanized regions of eastern India. In this study, two different years viz. 1993 and 2018 have been taken for the preparation of LULC and land surface temperature map. The kappa coefficient has been implied in this investigation to assess the accuracy of LULC maps. Temperature maps show that summer and winter surface temperature increases at the rate of 0.15 °C and 0.19 °C per year respectively. The result also reveals that temperature mainly increases due to the presence of urban, industrial and coal mine areas. The changing land use and land cover patterns show that the coal mine areas have been increased by 15% and urban areas also increased by 60%. Some correlations have been prepared to show the relationship between Land Surface Temperature (LST) and other spatial indices like NDBI, NDVI, and NDWI, where negative correlation prevails between LST and NDVI also with NDWI, but positive relation exists between LST and NDBI. Lastly, simulation of temperature for the year 2041 has been prepared, which shows that in the upcoming years' temperature may be increased up to 0.21 °C/year.

© 2020 National Authority for Remote Sensing and Space Sciences. Production and hosting by Elsevier B.V. This is an open access article under the CC BY-NC-ND license (<http://creativecommons.org/licenses/by-nc-nd/4.0/>).

### 1. Introduction

For proper identification of a region, Land use and Land cover (LULC) is one of the most vital parameters for the proper identification of a region (Rousta et al., 2018). Rapid transformation from pervious surface to impervious surface through LULC changes has a great impact on local as well as regional environment (Rousta et al., 2018; Zhou et al., 1998). So, the formation of urban heat islands is the most important striking feature of rapid urban and industrial growth in the present era of development (Ranagalage et al., 2018). Buildings, roads, industrial farms, etc. are considered as the impervious surface, which can absorb shortwave incoming solar radiation in one hand but on the other hand, it leads to a reduction in the outgoing longwave terrestrial emission (Ranagalage et al., 2018).

Several studies established that there is a strong influence of LULC on surface temperature and reported that the relative rise in LST depends on LULC change especially in the urban centers (Pal and Ziaul, 2017; Weng et al., 2004). Extension of agricultural land, the concretization of the open land, squeezing of surface water area, depletion of groundwater resources (Das and Mukhopadhyay, 2018), reduction of green vegetation area completely changes the existing environment (Zhang and Huang, 2015; Mahato and Pal, 2018). The negative effect of these kinds of change directly related to health risks & environment (Pal and Ziaul, 2017; Choudhury et al., 2019).

Remote Sensing and geospatial technology are some of the major modern tools for the identification of LULC and extraction of land surface temperature (LST) (Choudhury et al., 2019). Therefore, using both of these technologies, we can properly explain LULC changes as well as to extract the difference in land surface temperature (Hathout, 2002).

This paper attempt to identify the research objectives: (1) To detect the LULC changes over the last 23 years (2) To assess the Spatial as well as the temporal variation of surface temperature

Peer review under responsibility of National Authority for Remote Sensing and Space Sciences.

\* Corresponding author.

E-mail address: [niladridas123@gmail.com](mailto:niladridas123@gmail.com) (N. Das).

with the changing Land use. (3) To establish the correlation between LST and other spatial indices.

## 2. Materials and methods

### 2.1. Description of the test area

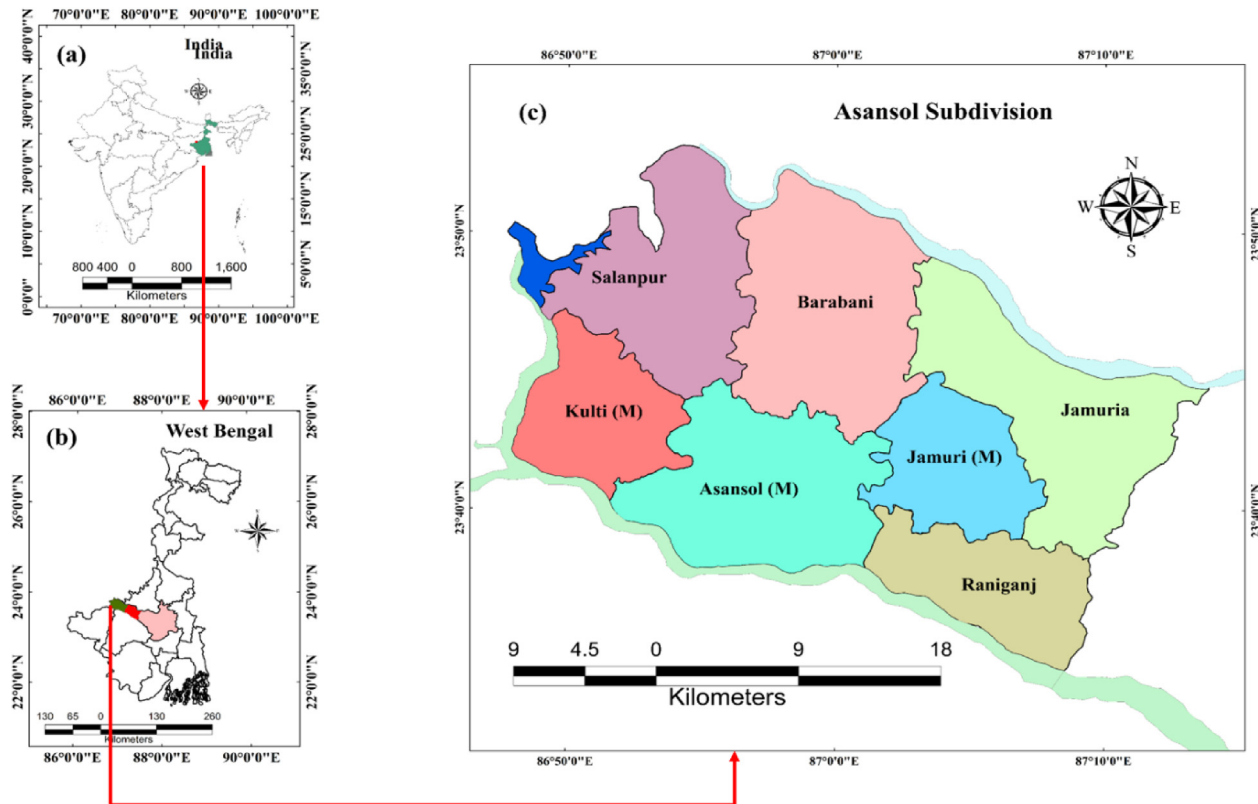
Asansol sub-division is lying on the Western part of the Asansol Durgapur Planning Area (ADPA). It occupies 836.80 Km<sup>2</sup> areas and had a population of 16.72 lakhs in 2011. The southern and northern part of the study area is bounded by Ajay and Damodar River.

The spatial extension of the study area is present between 23°41' 30" N to 23°53'30" N and 86°47' 41" E to 87°14' 04" E (Fig. 1).

The test area is experienced by tropical monsoon climate with high temperatures in the summer and dry winter season. The average rainfall is 1408 mm.

### 2.2. Database and methods

LANDSAT TM (path/row: 139/44; spatial resolution 30 m) data of 1995 and LANDSAT 8 OLI (path/row: 139/44; spatial resolution 30 m) data have been acquired from USGS earth explorer. The

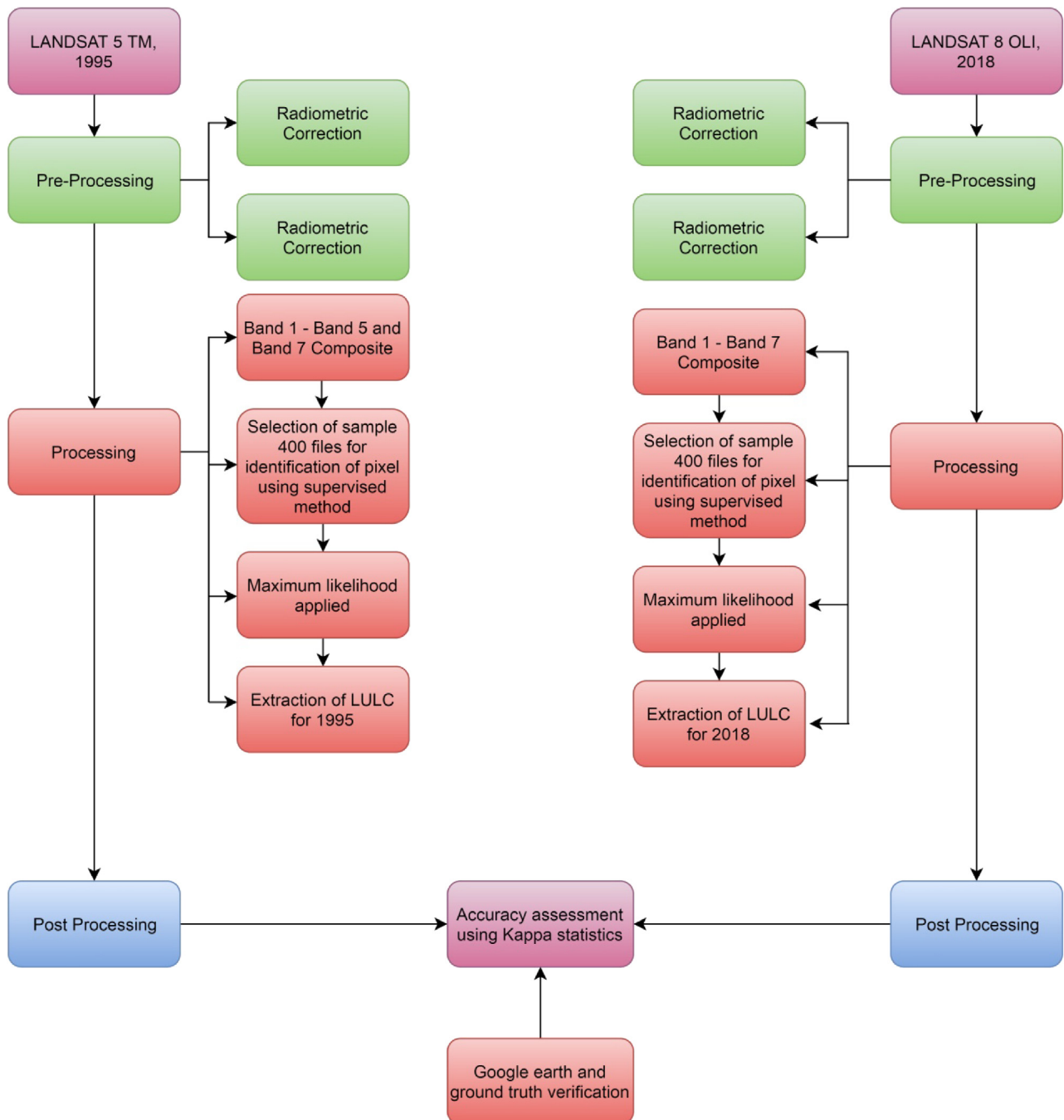


**Fig. 1.** Location of a. India, b. West Bengal and c. Asansol Subdivision.

**Table 1**

Specification of satellite data Landsat 5 (TM) and Landsat 8 (OLI).

Satellite	Sensor	Path/Row	Year	Band	Resolution	Wavelength ( $\mu\text{m}$ )	Band information (m)
Landsat-5	TM (Thematic Mapper)	139/44	1995	1	30	0.45–0.52	Visible Blue
				2	30	0.52–0.60	Visible Green
				3	30	0.63–0.69	Visible Red
				4	30	0.76–0.90	NIR
				5	30	1.55–1.75	SWIR 1
				6	120	10.40–12.50	Thermal
				7	30	2.08–2.35	SWIR 2
Landsat-8	OLI (Operational Land Imager) and TIRS (Thermal Infrared Sensor)	139/44	2018	1	30	0.43–0.45	Band 1 – Coastal aerosol
				2	30	0.45–0.51	Band 2 – Blue
				3	30	0.53–0.59	Band 3 – Green
				4	30	0.64–0.67	Band 4 – Red
				5	30	0.85–0.88	Band 5 – Near Infrared (NIR)
				6	30	1.57–1.65	Band 6 – SWIR 1
				7	30	2.11–2.29	Band 7 – SWIR 2
				8	15	0.50–0.68	Band 8 – Panchromatic
				9	30	1.36–1.38	Band 9 – Cirrus
				10	100	10.6–11.19	Band 10 – Thermal Infrared (TIRS) 1
				11	100	11.50–12.51	Band 11 – Thermal Infrared (TIRS) 2

**Fig. 2.** Procedures for land use and land cover classification.

acquired data were inbuilt georeferenced to UTM zone 45 North projection with WGS-84 datum (see band details in [Table 1](#)).

**Table 2**  
Remarks of the agreement for Kappa coefficient.

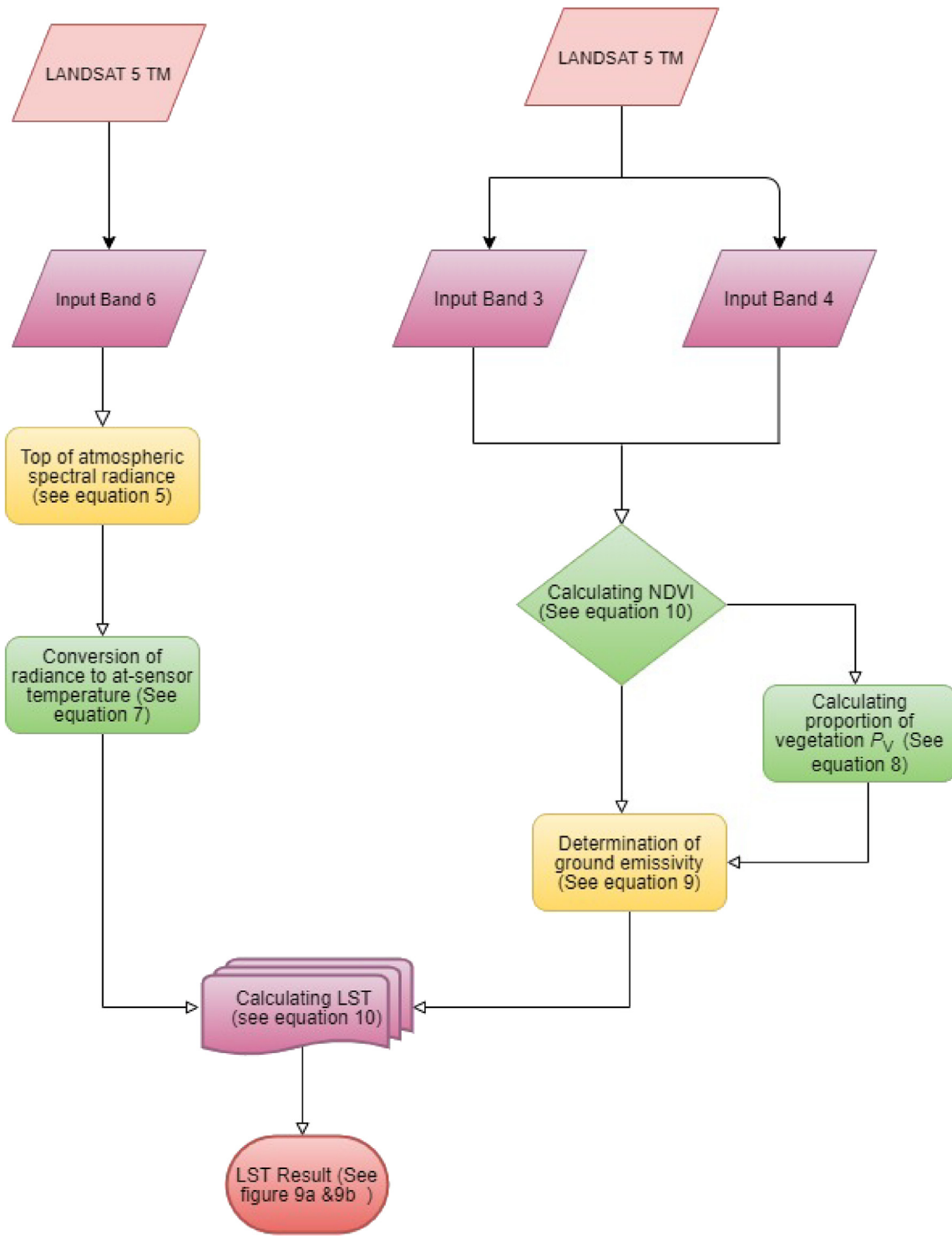
Value of Kappa-hat	Nature of agreement
$0.8 \leq \hat{K} \geq 1$	Almost perfect agreement
$0.61 \leq \hat{K} \geq 0.80$	Substantial agreement
$0.41 \leq \hat{K} \geq 0.60$	Moderate agreement
$0.21 \leq \hat{K} \geq 0.40$	Fair agreement
$\leq \hat{K} \geq 0.20$	Slight agreement
$\hat{K} < 0.00$	Poor agreement

**Source:** Bogoliubova & Tymkow, 2014.

#### 2.2.1. Method for land use and land cover classification from Landsat (TM/OLI) imagery

LULC map has been classified with the help of supervised classification using the maximum likelihood method of Image Classification tool in ArcGIS 10.5.

Band 1–5 and band-7 of Landsat-5 TM imagery have been considered for land use classification, but band 6 has been excluded as it denotes thermal band. Contrarily for Landsat-8 OLI imagery, bands 1–7 have been taken into consideration for land use classification. For the preparation of land use and land cover maps, all the bands have been stacked in ArcGIS 10.5 software using image analyst tool, then training sample manager tool has been used to identify the signature of the pixels, for this purpose large number of training samples have been collected randomly from the entire

**Fig. 3.** Extraction of LST from Landsat TM.

imagery. The entire procedure for land use classification has been shown through the flow chart (Fig. 2).

#### 2.2.2. Method of accuracy assessment of land use maps

In this study, accuracy assessment has been made through the confusion matrix or error matrix. This matrix explains the information about the actual and predicted identification of the pixel (Jupp, 1989; Pal and Ziaul, 2017). To calculate the overall accuracy, this formula has been used-

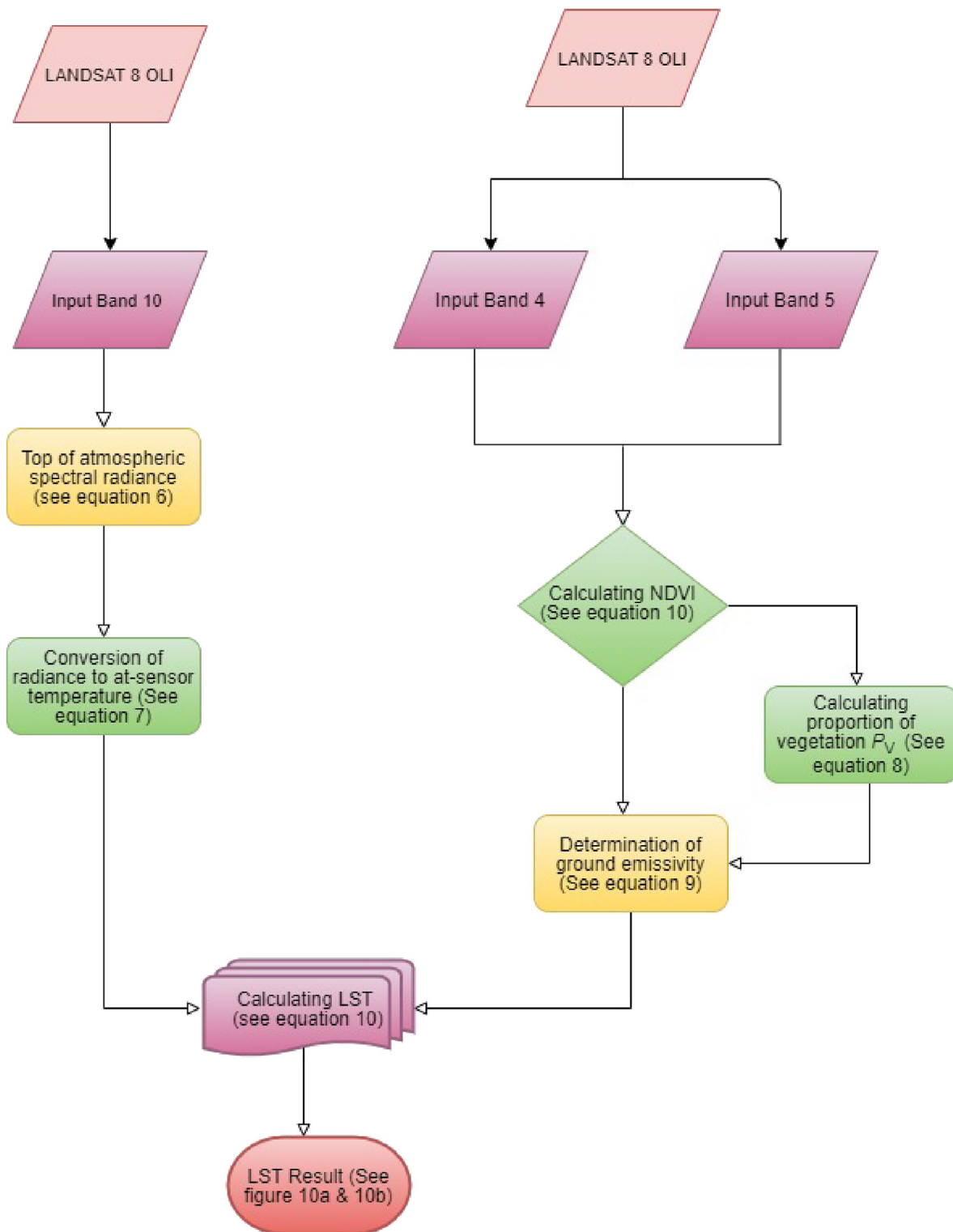
$$T = \frac{\sum D_{ii}}{N} \quad (1)$$

where

T – Overall accuracy

$\sum D_{ii}$  – the total number of correctly classified pixels

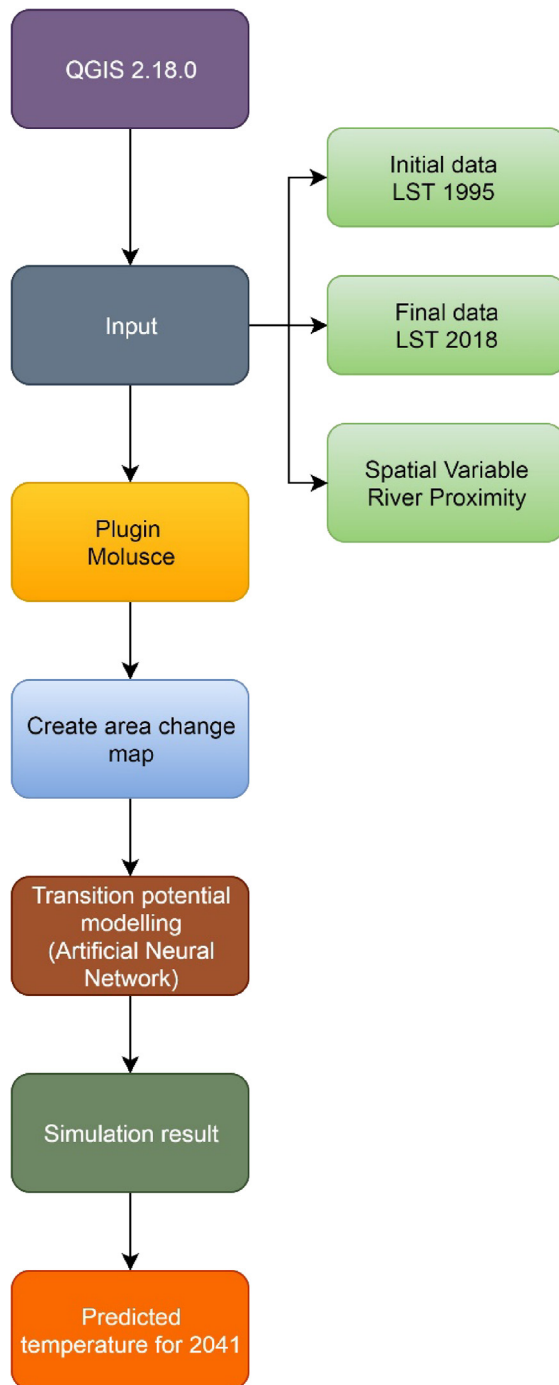
N – total number of pixels in the error matrix

**Fig. 4.** Extraction of LST from Landsat OLI.**Table 3**  
Thermal Constant of Landsat TM & OLI thermal imageries.

Sensor	Year	Band	K <sub>1</sub>	K <sub>2</sub>
Landsat TM	1995	Band 6	607.76	1260.56
Landsat OLI	2018	Band 10	774.8853	1321.0789

**Table 4**  
Values of NDVI and associated information.

NDVI values	Information
-1	Water bodies
-0.1 to 0.1	Barren areas of rock, sand or snow
0.2 to 0.4	Shrub and grassland
+1	Temperate & tropical forest

**Fig. 5.** Preparation of Predicted LST map in Q.GIS.

In this study, a total of 400 sample sites have been created for the ground truth verification from the Google earth and the actual ground using Global Positioning System (GPS) for the accuracy assessment (Ranagalage et al., 2019). Two other methods have also been applied, the producer's accuracy is a form of referenced based accuracy which has been computed by reviewing the predictions produced for a class and it is expressed as a percentage. Another the user's accuracy is a form of map-based accuracy that calculated by reviewing the referenced data of a class and it has also been expressed in percentage (Story and Congalton, 1986). Producer's accuracy and user's accuracy can be obtained from the following formulas:

$$PA = \frac{\sum D_{ij}}{R_i} \quad (2)$$

where

PA – Producer's accuracy  
 $D_{ij}$  - number of correctly classified pixels in row i (in the diagonal cell)  
 $R_i$  - total number of pixels in row i

$$UA = \frac{\sum D_{ij}}{C_j} \quad (3)$$

where

UA – User's accuracy  
 $D_{ij}$  - number of correctly classified pixels in column j (in the diagonal cell)  
 $C_j$  - total number of pixels in column j

Except, the above methods, another accuracy coefficient which is known as Kappa coefficient or Kappa hat or K-hat ( $\hat{K}$ ) (Foody, 1992) has been implied in this study. The K value ranges between 0 and 1, where 0 represents poor agreement and 1 represents almost perfect agreement. Interpretation of the agreement of kappa has been described by Landis and Koch (1977) (Table 2). The kappa coefficient formula is given below [4].

$$\hat{K} = \frac{N \sum_{i=1}^m D_{ij} - \sum_{i=1}^m R_i C_j}{N^2 - \sum_{i=1}^m R_i C_j} \quad (4)$$

where

$\hat{K}$  – Kappa-Coefficient  
N – Total number of pixels  
m – Number of classes  
 $\sum D_{ij}$  – Total diagonal elements of an error matrix (the sum of correctly classified pixels in all images)  
 $R_j$  – Total number of pixels in row i  
 $C_j$  – Total number of pixels in column j

Kappa statistic (Cohen, 1960) is considered the most experienced measures of accuracy of LULC maps as it provides much better interclass discrimination than the overall accuracy (Foody, 1992). In this study to run Kappa statistic 400 sample sites from the entire map have been selected and 50 sample sites from each category have been taken into consideration.

### 2.2.3. Extraction methods of LST from the thermal band

The temperature of the ground surface has been derived from the thermal bands of Landsat-5 TM (band 6) and Landsat-8 OLI (band 10) for May as summer season and December as winter season.

But the extraction process of LST from Landsat TM and Landsat OLI is slightly different in terms to calculate spectral radiance ( $L_s$ ). The procedures for the extraction of LST has been described in detail by many articles (Asgarian et al., 2014; Govind and Ramesh, 2019) Figs. 3 and 4 depicts the stepwise extraction of LST from Landsat TM and Landsat OLI imagery.

#### 2.2.3.1. Step-I: Conversion of digital number (DN) to radiance/conversion to top of atmosphere (TOA) radiance ( $L_s$ ). For Landsat- 5 TM ima-

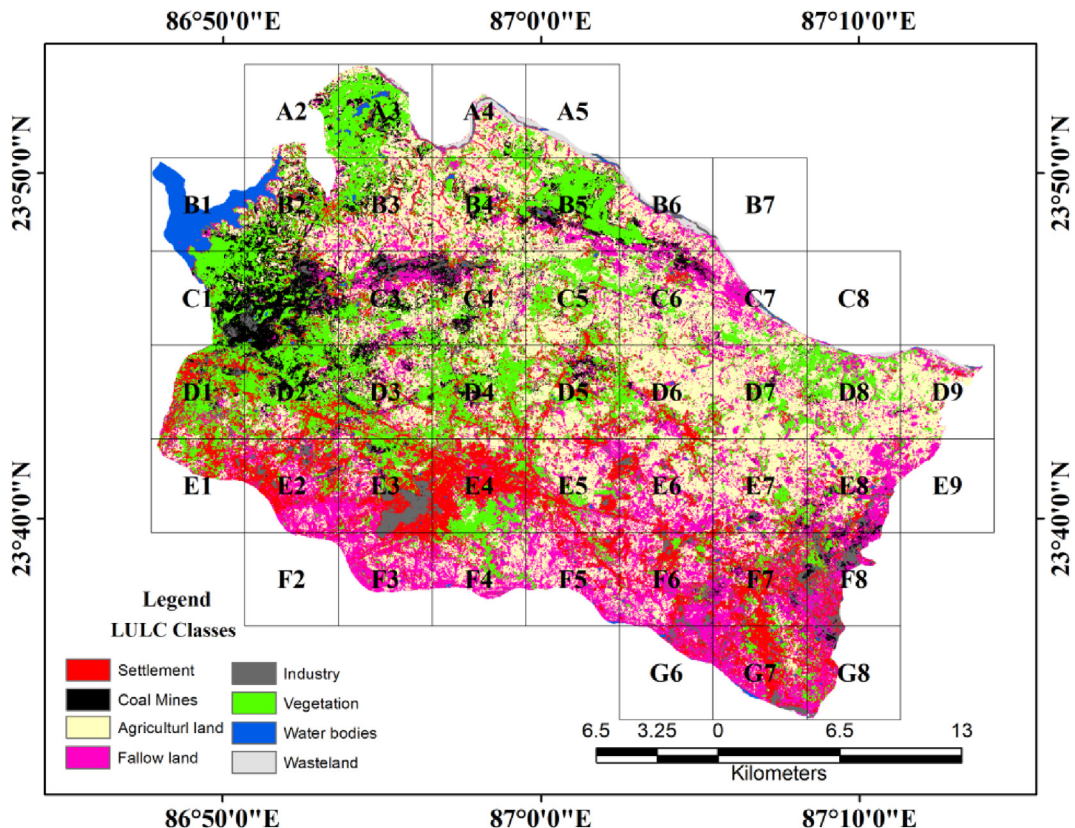


Fig. 6. Grid wise land use/ land cover map of 1995.

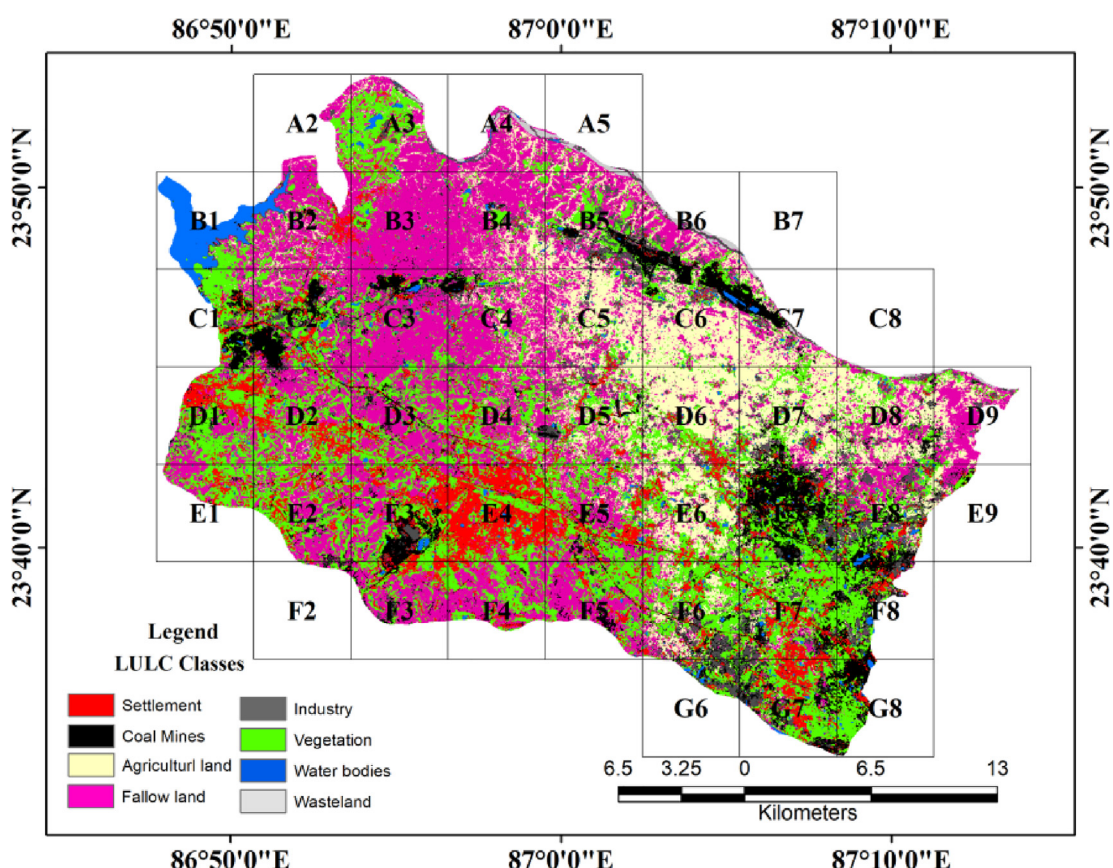


Fig. 7. Grid wise land use/ land cover map of 2018.

gery band 6 has been used as a thermal band and the following equation has been used to calculate spectral radiance ( $L\lambda$ ) [5]

$$L\lambda = LMIN\lambda$$

$$+ [(LMAX\lambda - LMIN\lambda)/(QCALMAX - QCALMIN)] \times QCAL \quad (5)$$

where QCALMIN = 1, QCALMAX = 255, QCAL = Digital Number of each pixel,  $LMAX\lambda$  &  $LMIN\lambda$  are the spectral radiances for the band 6 at digital number. The value of  $LMAX\lambda$  = 15.303 and  $LMIN\lambda$  = 1.238.

For Landsat-8 OLI imagery band 10 is the thermal band and to extract spectral radiance ( $L\lambda$ ), the following equation has been implied [6]

$$L\lambda = ML * QCAL + AL \quad (6)$$

where

$L\lambda$  = Spectral Radiance of top of the atmosphere

$M_L$  = the band-specific multiplicative rescaling factor (0.0003342)

$AL$  = the band-specific additive rescaling factor (0.1)

QCAL = Quantized and Calibrated Standard Product Pixel value (band 10 image)

2.2.3.2. Step-II: Transformation of spectral radiance to At-satellite brightness temperatures (BT). After the conversion of the digital number into radiance, the data has now converted into brightness temperature (BT) utilizing thermal constant given in the metadata file. Following equation in the tool's algorithm to convert reflectance to BT [7]

$$BT = \left( \frac{K_2}{\ln[(K_1/L\lambda) + 1]} \right) - 273.15 \quad (7)$$

where

BT = At-satellite brightness temperature

$L\lambda$  = TOA spectral radiance [vide equation (6)]

$K_1$  = Band constant (Table 3)

$K_2$  = Band constant (Table 3)

273.15 helps to convert the temperature from Kelvin to Celsius.

2.2.3.3. Step-III proportion of vegetation ( $P_V$ ). Normalized Difference Vegetation Index (NDVI) is the main parameter to calculate the proportion of vegetation. It has been calculated as following [8]

$$PV = \left( \frac{NDVI - NDVI_{min}}{NDVI_{max} - NDVI_{min}} \right)^2 \quad (8)$$

2.2.3.4. Step-IV Emissivity correction ( $\varepsilon$ ). Now, we can easily correct the emissivity ( $\varepsilon$ ) with the help of the following equation [9]

$$\text{Land surface emissivity } (\varepsilon) = 0.004 * PV + 0.986 \quad (9)$$

#### 2.2.3.5. Step-V Calculation ground surface temperature.

$$LST = \frac{BT}{\left[ 1 + \left\{ \left( \lambda * \frac{BT}{\rho} \right) * \ln \varepsilon \right\} \right]} \quad (10)$$

where

LST = Land Surface Temperature  $\lambda$  = wave length of emitted radiance in meters (Markham and Barker, 1985)  $\rho$  =  $h^*c/\sigma$

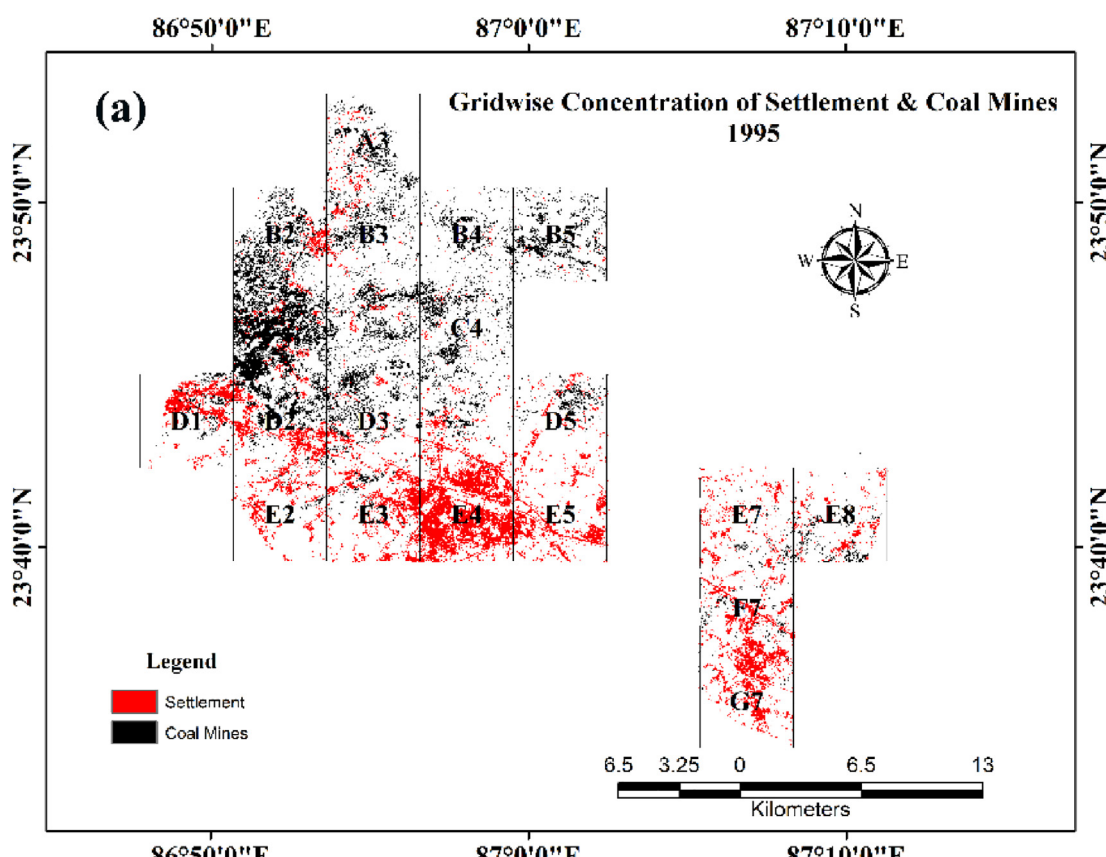
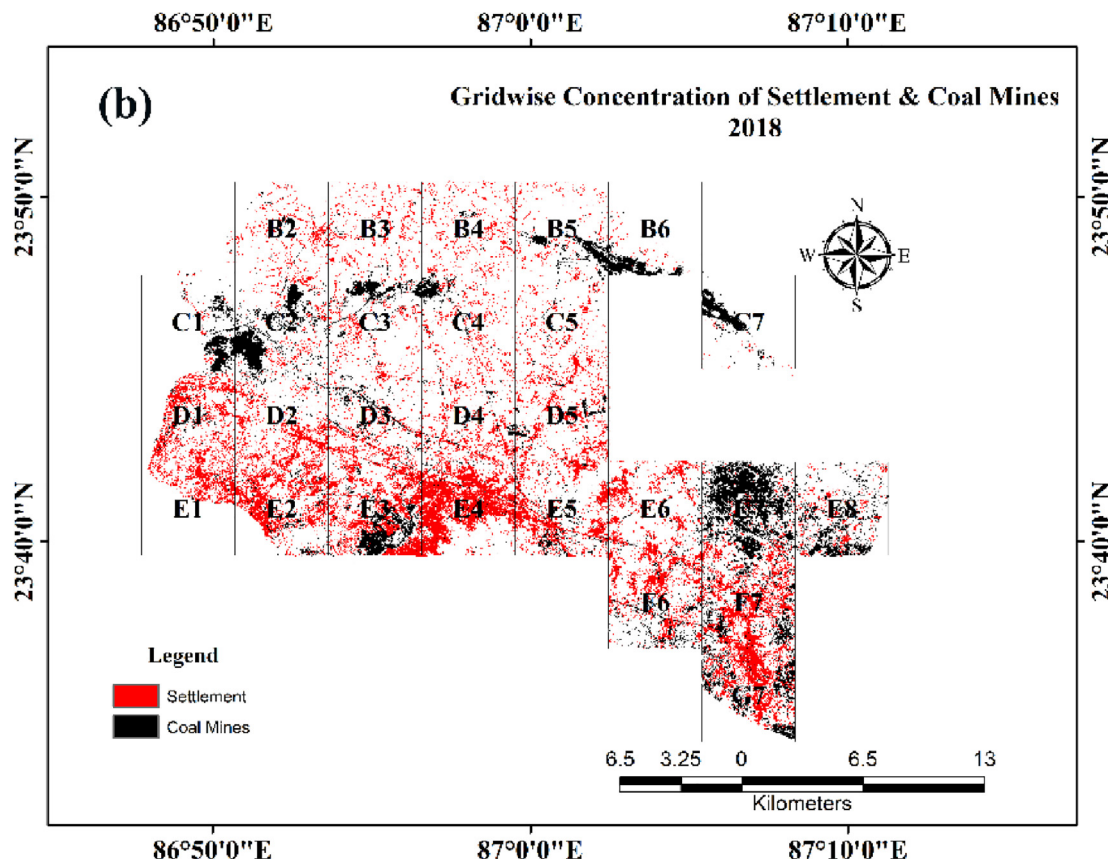


Fig. 8a. Gridwise settlement and coal mines concentration, 1995.

**Fig. 8b.** Gridwise settlement and coal mines concentration, 2018.**Table 5**

Accuracy assessment of land use and land cover of 1995 and 2018.

Year	Land use category	Class type determined from reference source									Kappa Co-efficient ( $\bar{K}$ )
		Settlement	Vegetation	Water Bodies	Agricultural land	Coal mines	Fallow land	Industry	Wasteland	Total	
1995	Settlement	40	0	0	5	2	2	0	1	50	80
	Vegetation	1	40	1	4	1	1	1	1	50	80
	Water Bodies	1	0	45	0	3	0	1	0	50	90
	Agricultural land	1	2	0	38	0	6	0	3	50	76
	Coal mines	1	1	1	0	42	0	5	0	50	84
	Fallow land	0	0	0	8	0	40	0	2	50	80
	Industry	1	0	1	1	2	0	42	3	50	84
	Wasteland	0	0	0	0	0	1	0	49	50	98
	Total	45	43	48	56	50	50	49	59	336	
	Producer accuracy	88.88	93.02	0.93	67.85	84	80	85.71	83.05	583.44	
2018	Overall accuracy (T)				84						0.81
	Settlement	45	0	0	1	2	2	0	0	50	90
	Vegetation	0	47	1	0	0	1	0	1	50	94
	Water Bodies	0	0	49	0	1	0	0	0	50	98
	Agricultural land	1	2	0	38	0	6	0	3	50	76
	Coal mines	0	1	1	0	48	0	0	0	50	96
	Fallow land	0	0	0	8	0	40	0	2	50	80
	Industry	1	0	1	1	2	0	42	3	50	84
	Wasteland	0	0	0	0	0	1	0	49	50	98
	Total	47	50	52	48	53	50	42	58	358	
	Producer accuracy	95.74	94	94.23	79.17	90.57	80	100	84.48	718.19	
	Overall accuracy (T)				0.89						

$(1.438 \times 10^{-2} \text{ m K})$ ,  $\sigma = \text{Boltzmann constant}$  ( $1.38 \times 10^{-23} \text{ J/K}$ ),  $h = \text{Planck's constant}$  ( $6.626 \times 10^{-34} \text{ J s}$ ),  $c = \text{velocity of light}$  ( $2.998 \times 10^8 \text{ m/s}$ ) and  $\epsilon = \text{emissivity}$  (ranges between 0.97 and 0.99).

#### 2.2.4. Methods for calculation of various spatial indices

Land Surface Temperature has been associated with the Normalized Difference Vegetation Index (NDVI), Normalized Difference Water Index (NDWI) and Normalized Difference Built-up Index (NDBI).

NDVI is the difference between near-infrared and red reflectance which is the divisible sum of two and it describes vegetation phenology (Dissanayake et al., 2019). NDVI has been extracted with the aid of the following method (Townshend and Justice, 1986) [11].

$$\text{NDVI} = \frac{(\text{NIR band} - \text{R band})}{(\text{NIR band} + \text{R band})} \quad (11)$$

where NIR means Near Infrared band and R means Red band. For Landsat TM band 4 and band 3 and for Landsat OLI band 5 and band 4 have been used to extract NDVI. The value of NDVI ranges from  $-1$  (Negative) to  $+1$  (Positive), where Negative values of NDVI indicates water and positive values correspond to vegetation (Table 4).

NDWI is another index that is used to demarcate open water and improve their existence through remote sensing data based

on near-infrared and visible radiation. NDWI can be derived with the following formula (McFeeters, 1996) [12]

$$\text{NDWI} = \frac{(\text{Green band} - \text{NIR band})}{(\text{Green band} + \text{NIR band})} \quad (12)$$

where the green band is band 2 for Landsat TM imagery and band 3 for Landsat OLI imagery. Near-Infrared (NIR) band is band 4 for Landsat TM and band 5 for Landsat OLI.

Values of NDWI lie between  $-1$  to  $1$ . In the case of water bodies, NDWI value is  $>0.5$  and smaller values like negative values correspond to vegetation, so it is easy to distinguish water bodies from vegetation. The values range from  $0$  to  $0.2$  corresponds to the built-up features.

Remote sensed data help us to calculate the built-up index using the Middle infrared band (MIR) and near-infrared band (NIR). NDBI has been derived using the following equation (Zha et al., 2003) [13]

$$\text{NDBI} = \frac{(\text{MIR band} - \text{NIR band})}{(\text{MIR band} + \text{NIR band})} \quad (13)$$

where MIR is the middle infrared band (For Landsat TM it is band 5 and for Landsat OLI it is band 6) and NIR is the near-infrared band (For Landsat TM it is band 4 and for Landsat OLI it is band 5).

The values of NDBI also lies between  $-1$  to  $+1$ , where  $0$  to  $1$  correspond to built-up and value near  $1$  indicates a high density of built-up area (Choudhury et al., 2019).

#### 2.2.5. Method to identify the association between LST and other spatial parameters

To understand the influence of the different spatial parameters on Surface Temperature, Pearson's Product Moment correlation has been applied. In this study, raster-raster (e.g. LST and NDVI; LST and NDWI and so on) correlation has been calculated in QGIS 3.8.1 software (Discussed in result and analysis section) using scatter plot tool.

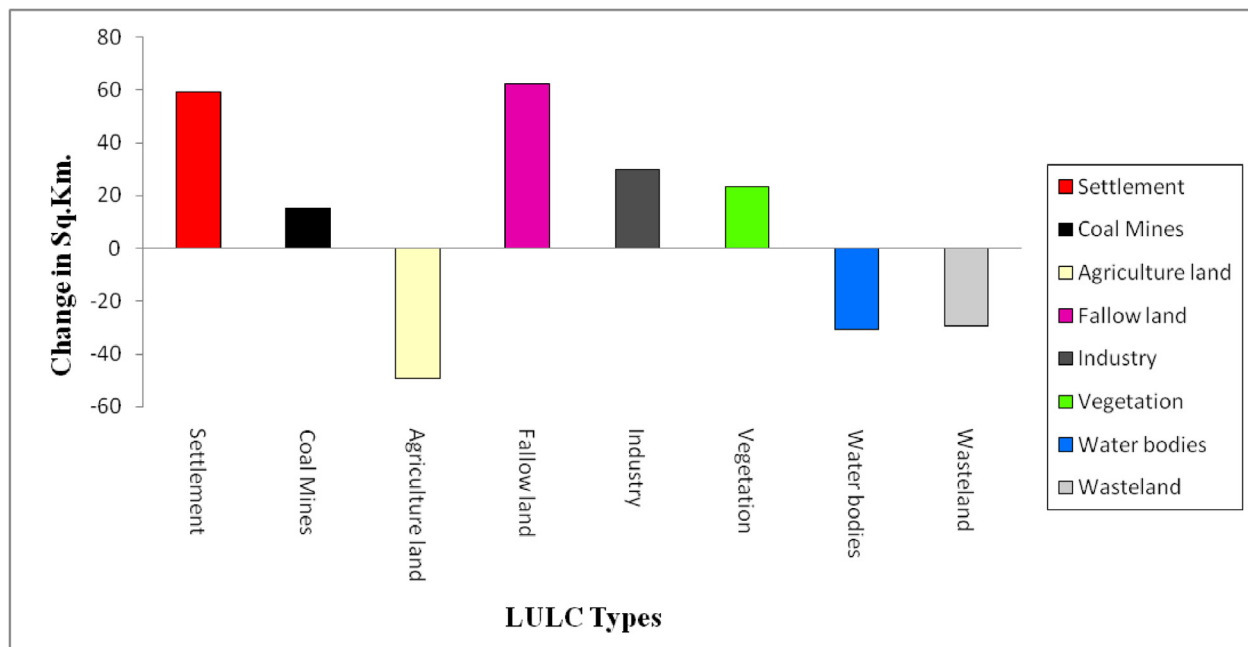


Fig. 9. Positive and negative Land use/ land cover area between 1995 and 2018.

**Table 7**  
Change of LULC area between 1995 and 2018.

LULC Category	Change (in %)
Settlement	59.29162902
Coal Mines	15.28105376
Agriculture land	-49.41563511
Fallow land	62.37780445
Industry	29.99824738
Vegetation	23.28817198
Water bodies	-30.76527382
Wasteland	-29.27156264

#### 2.2.6. Method for change detection

Land use and land cover classification of 1995 and 2018 have been compared using the change matrix (Weng et al., 2004) in Arc Gis 10.5 software. Both qualitative and quantitative methods have been used to identify change detection. After the detection of the change matrix, a change map has been generated in the Arc Gis environment using spatial analysis tool (Detail discussion is in result and analysis section).

#### 2.2.7. Method to estimate the predicted temperature

It is an important part of the study, where the future temperature has been predicted for the next 23 years through simulation. There are several methods to predict simulated temperature like Artificial Neural Networks, Markov chain, hybrid neural model, regression model, etc (Bhattacharjee et al., 2014; JokarArsanjani et al., 2013; Saba et al., 2017; Tetteyet et al., 2017; San and Khin,

2016; Fahimi Nezhad et al., 2019). In this study Q. GIS has been implied to predict future temperature. Molusce tool in Q.GIS helps to formulate this model. The procedure to prepare the predicted LST map has been shown in the following flow chart (Fig. 5).

### 3. Result and discussion

#### 3.1. Land use and land cover change analysis

The LULC maps have been categorized into eight classes viz. settlement, water bodies, coal mines, agricultural land, fallow land, industry, vegetation, and wasteland. In 1995 major coal mines area has been observed in the C2 grid (Figs. 6 and 8a) but it extends in Grid B6, E7 & E3 and reduce in C2 grid and converted to wasteland in 2018 (Figs. 7 and 8b). The area under each LULC category has been depicted in Table 5. If we look on settlement concentration, it can be observed that settlement are mainly concentrated on E4 grid in 1995 but in 2018 settlement are expand and concentrated on D1, E2, E7 & F7 Grid (Figs. 8a & 8b). Land use and land cover area for each category for both year has been shown in Table 6.

The accuracy assessment of LULC has also been analyzed with the help of the Kappa coefficient (Vide methodology; equation (4)).

For the LULC of 1995, the value of Kappa was 0.81 and for 2018 the kappa value was 0.88 (Table 5) which means both the land use and land cover classification can be interpreted as almost perfect agreement (Table 2).

Fig. 9 shows the positive and negative change of land use and land cover of eight classes, where settlement, coal mines, fallow

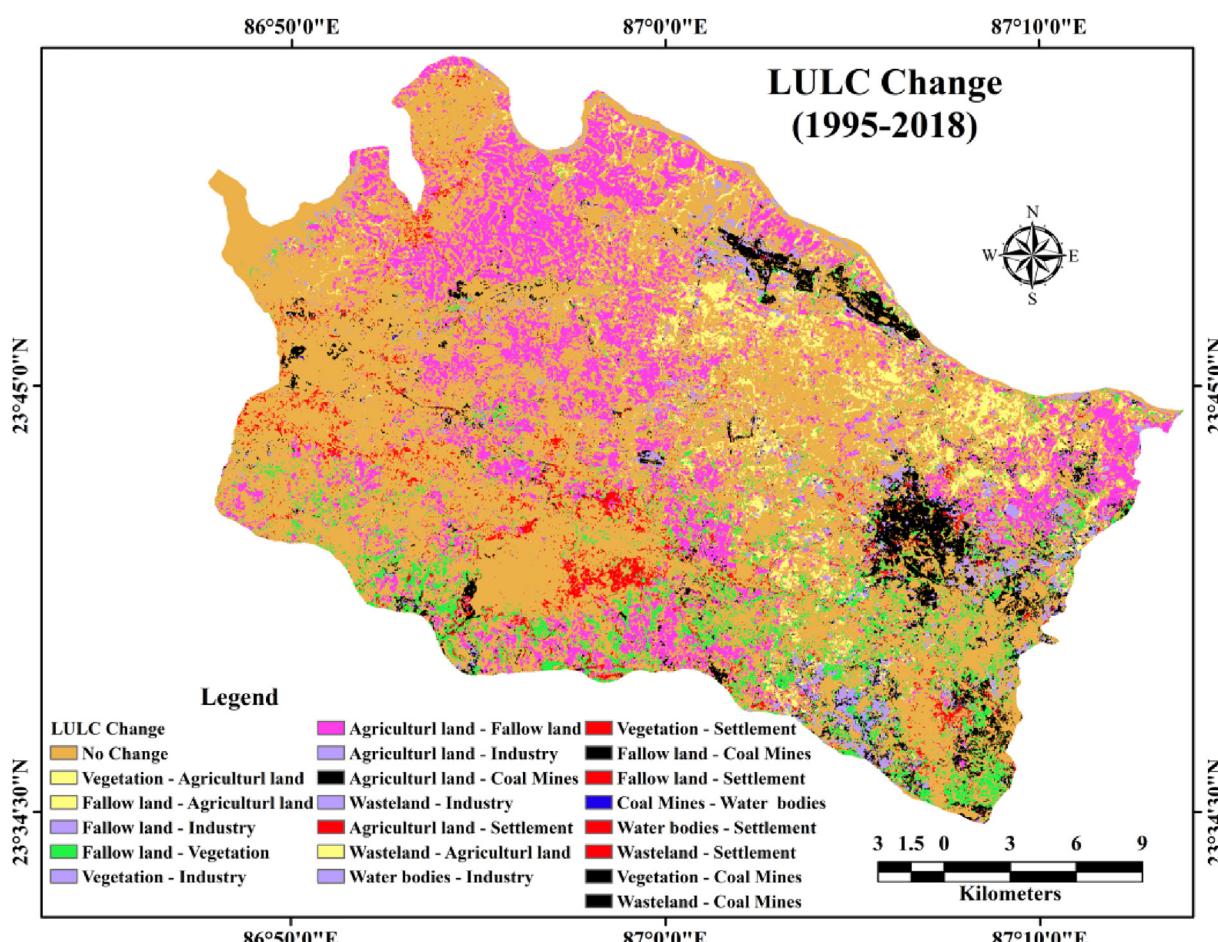


Fig. 10. Land use/land cover change map (1995–2018).

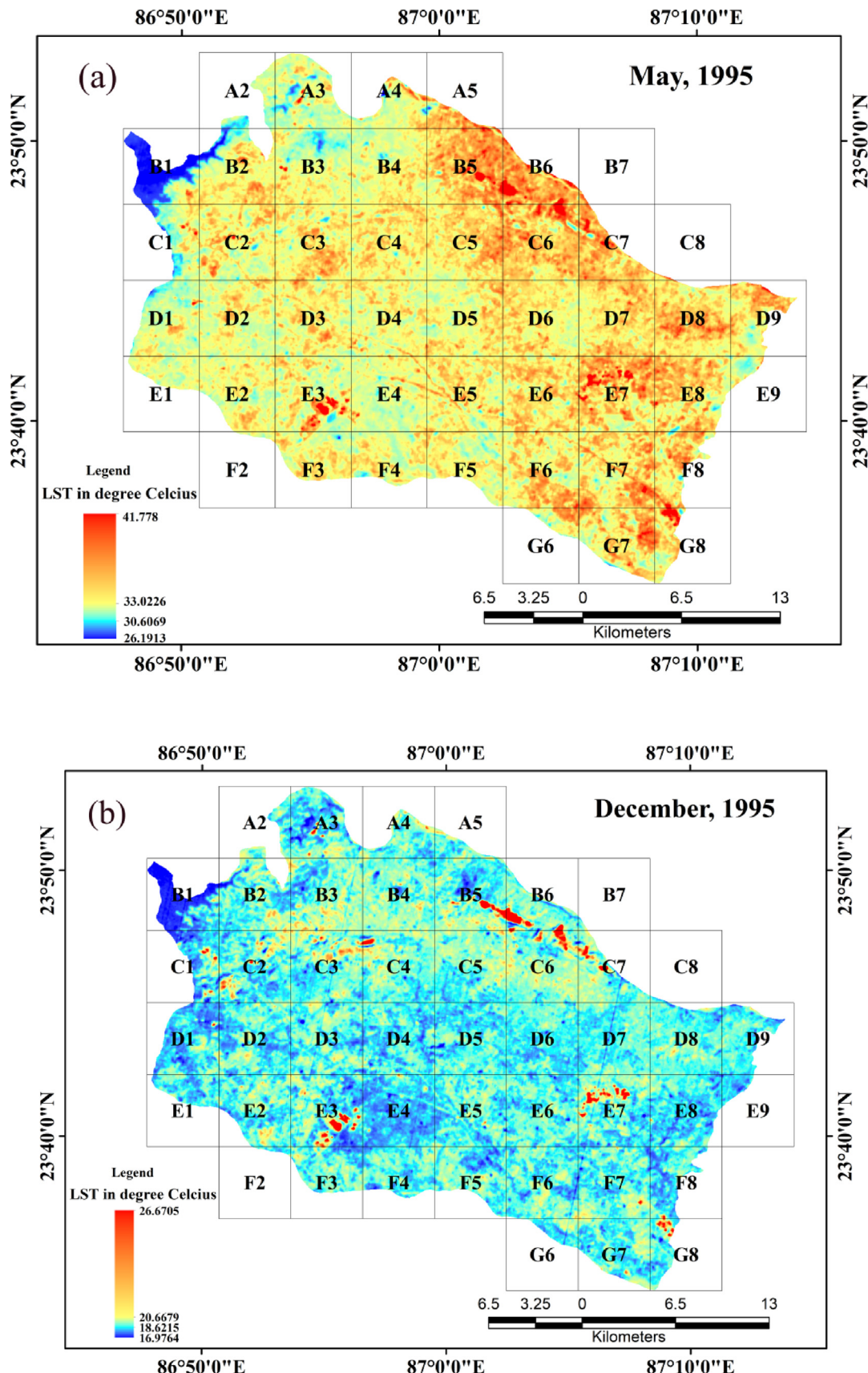


Fig. 11. (a) LST of May 1995 (b) LST of December 1995.

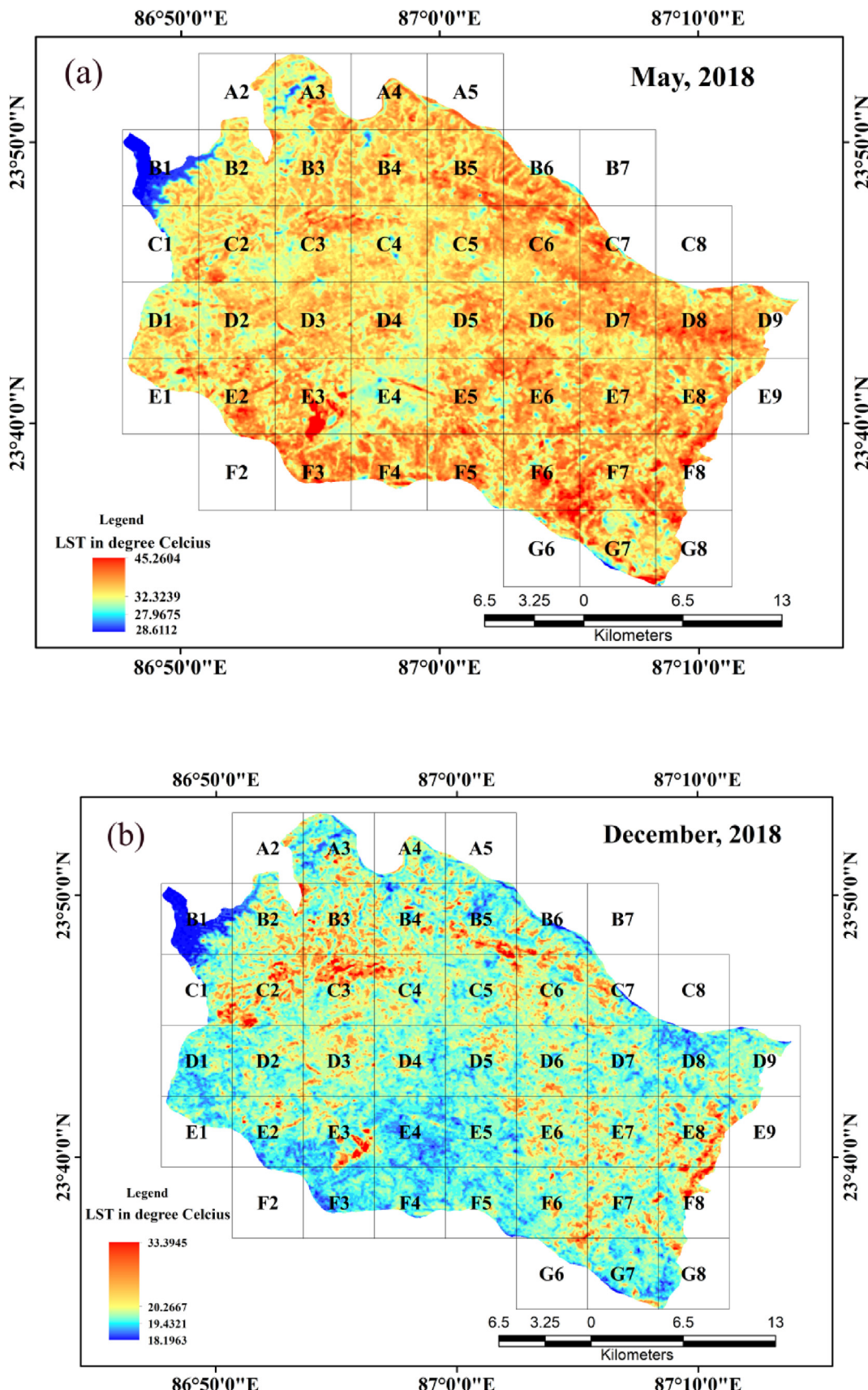
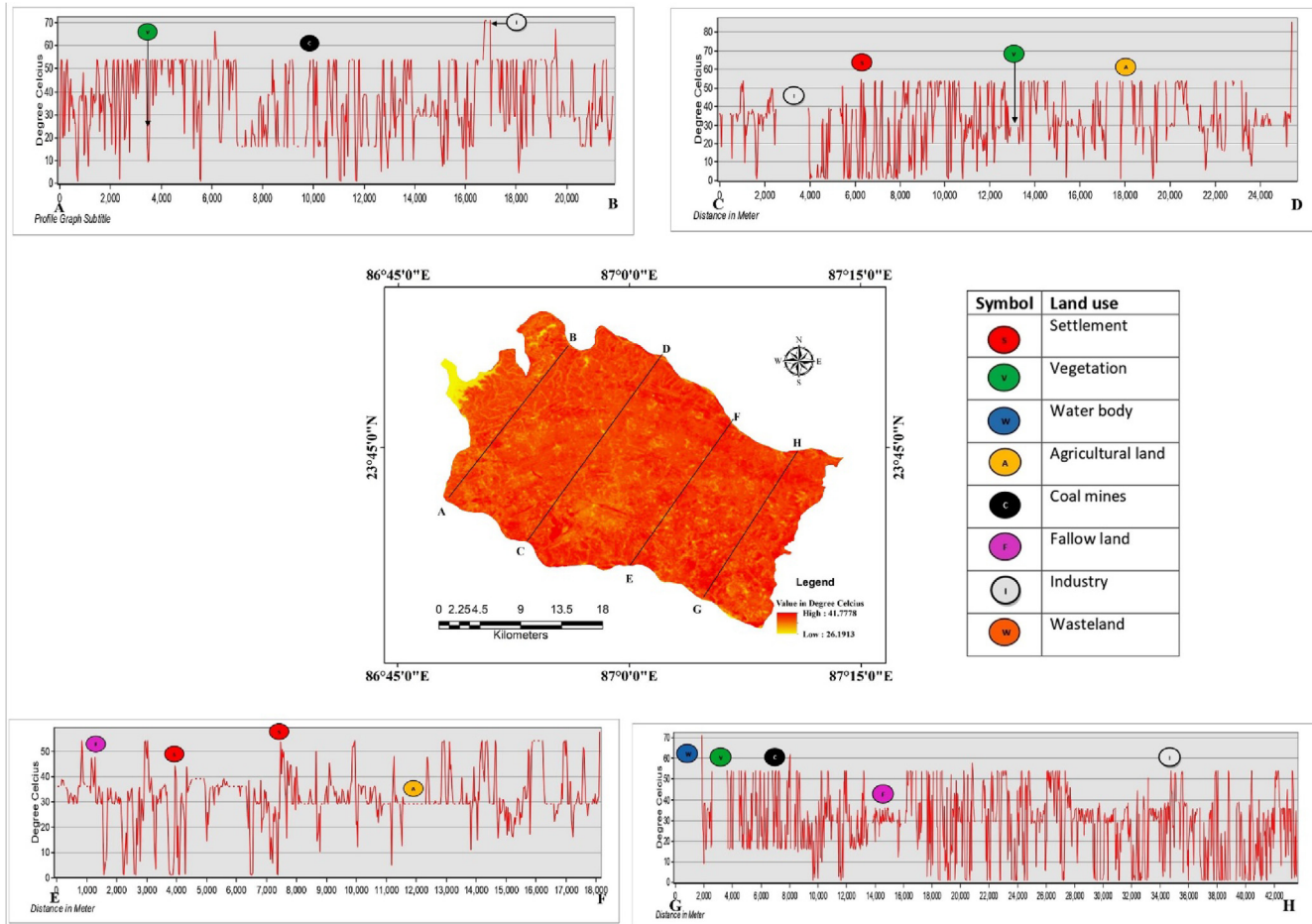


Fig. 12. (a) LST of May 2018 (b) LST of December 2018.

**Table 8**

Season wise temperature data and rate of temperature change.

Month	Season	year	Maximum temperature (°C)	Minimum temperature (°C)	Average temperature (°C)	Rate of change (°C)/year
May	<b>Summer</b>	1995	41.778	26.1913	33.98465	<b>0.12831</b>
		2018	45.2604	28.6112	36.9358	
December	<b>Winter</b>	1995	26.6705	16.9764	21.82345	<b>0.17269</b>
		2018	33.3945	18.1963	25.7954	

**Fig. 13.** LST profiles along A-B, C-D, E-F, and G-H in May 1995.

land, industry, vegetation were changed positively and agricultural land, water bodies and wasteland were changed negatively (Table 7 and Fig. 9). Positive change means the area under land use and land cover has been increased and negative change indicates a reduction of land use and land cover areas. Settlement areas have been increased by 60% due to huge urbanization in this area and it results in the reduction of agricultural land and water bodies. Coal mines also have been increased by 15% (Fig. 9; Table 7), e.g. in B5 and B6 grid vegetation area has been converted into coal mines areas, which may increase surface temperature. It has been interestingly noted that vegetation areas have been increased up to 23.2% (Fig. 9; Table 7). The land use and land cover change map is shown in Fig. 10.

### 3.2. Land surface temperature change analysis concerning land use and land cover units

Change of Land surface temperature has also been extracted for the year 1995 and 2018 for summer and winter seasons [Figs. 11

(a), (b) and 12 (a), (b)]. For the summer season of 1995, the maximum temperature is 41.7 °C and the minimum temperature is 26.19 °C. But in 2018 surface temperature has increased both in summer and winter season. In summer 2018 the maximum temperature is 45.26 °C and the minimum temperature is 28.61 °C. So, it has been clear that the maximum temperature during summer and it has been increased up to 3.56 °C. The rate of change of temperature per year during summer and winter season between 1995 and 2018 is 0.12 °C and 0.17 °C respectively (Table 8).

At the micro-level, the climate has been changed with the changing of the LULC units. The rate of temperature change is very prominent at the impervious surface (Ranagalage et al., 2019). So, to catch on the correlation between LST and LULC units, four cross-sections (A-B, C-D, E-F, and G-H) have been drawn for each land surface temperature map (1995 and 2018) of the summer season (Figs. 13 and 14). Both the figure shows that in the impervious surface mainly in the built-up area temperature varies from 38 °C to 46 °C and high temperatures also prevail in the coal mine areas, where the temperature ranges between 42 °C to 46 °C. The indus-

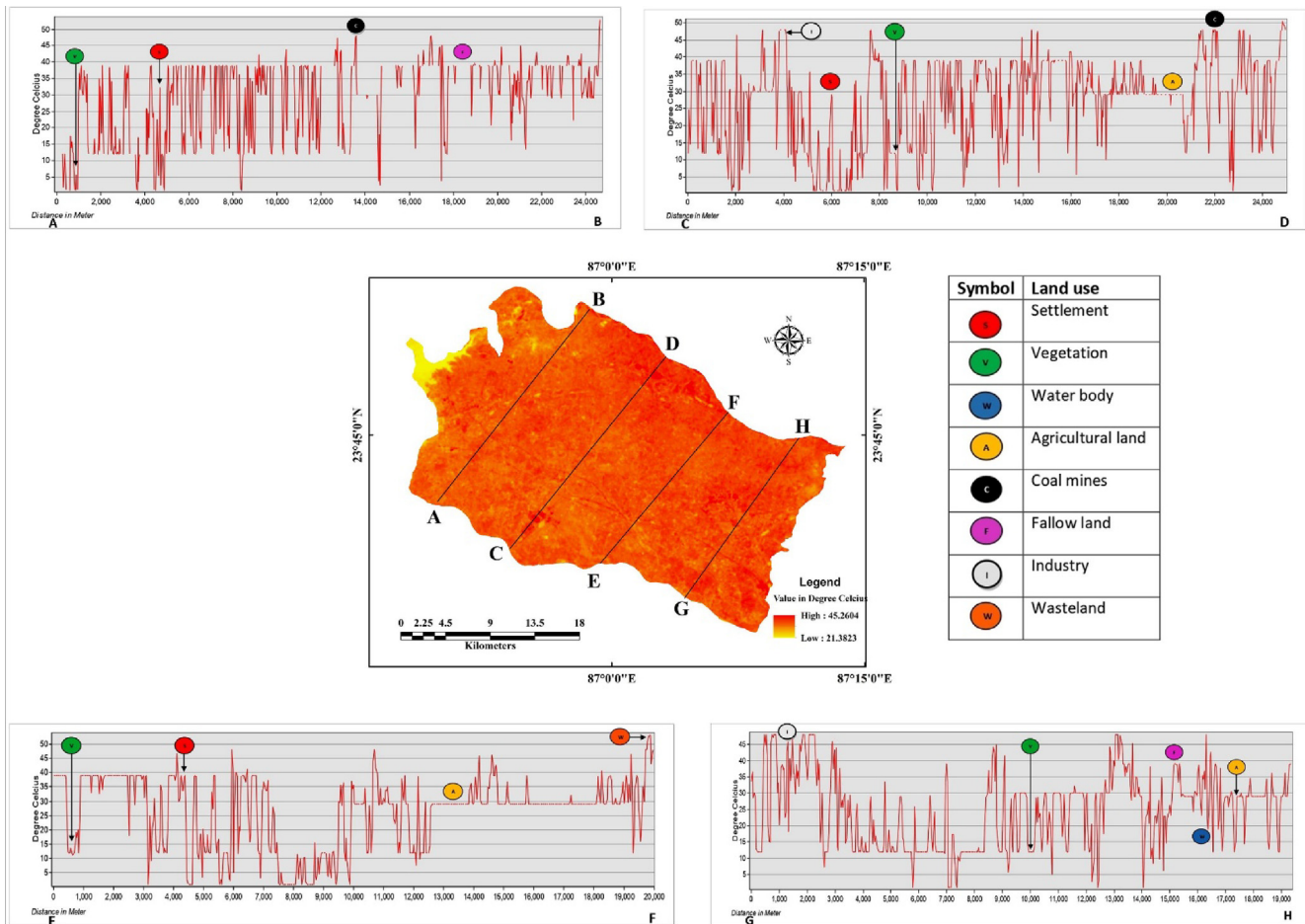


**Fig. 14.** LST profiles along A-B, C-D, E-F, and G-H in May 2018.

try is another land cover unit that is responsible for the hike of temperature. But in the vegetation unit, the temperature remains below 20 °C due to the high transpiration rate.

### 3.3. Impact of water bodies, vegetation and building area on land surface temperature

Other correlations have been studied between LST and water bodies, built-up areas and vegetation. All the maps have been prepared for the winter season as the winter season is cloud-free and low atmospheric haziness. Fig. 15 (a) and (b) depicts the spatial pattern of NDVI, where darker green shows dense vegetation cover and blue color shows the presence of water bodies and light green shows built-up areas. NDVI 1995 reveals that the B5 grid has dense vegetation cover and E3 and E4 have very low vegetation cover due to the extension of the urban area. In this connection, a relation can be established between NDVI and NDBI. Fig. 16 shows that there is a very high negative correlation ( $-0.95$ ) between NDBI and NDVI which means massive urbanization leads to the reduction of vegetation land. Fig. 17(a) and (b) also represent negative relation between NDVI and LST for both 1995 and 2018 because dense vegetation do not allow to receive more temperature by the earth's surface.

NDWI is also another important index which is directly related to land surface temperature. There is a very high negative correlation ( $-0.9$ ) (Table 9) between them as the specific heat of water is very high (Hirasawa and Urakami, 2010; Moldoveanu and Minea,

2019) moreover, NDWI highly determines the LST (Fig. 18) (see Table 10).

Another important relationship has been observed between NDBI and NDWI. NDBI negatively influences NDWI (Fig. 19) that means with the extension of the built-up area, surface storage becomes reduced. The correlation value between them is  $-0.85$  (Table 10).

The last index that is NDBI or Normalized Difference Built-up Index has a keen impact on ground surface temperature. The relational value between them is  $0.93$  (Tables 9 and 10) that refers to a very high positive relation (Fig. 20 a and b). Asansol sub-division is one of the most important industrial and mining regions. So, here it has been expected to increase the surface temperature with the increase of industrialization, urbanization, and concretization in the next few years.

### 3.4. Predicted temperature for 2041

This section is an important part of the study where temperature of 2041 has been predicted with the help of artificial Neural Network model in Q.GIS (Vide methodology). The predicted temperature reveals that temperature will be increased at the place where coal mines, industries and urban area are present. With the increase of human demand, coal mines, industries as well as urban area will rapidly increased in the test region, so there will be huge chance of increasing temperature of the above mention landuse regions. Both figures viz. Figs. 21a and 21b show the tem-

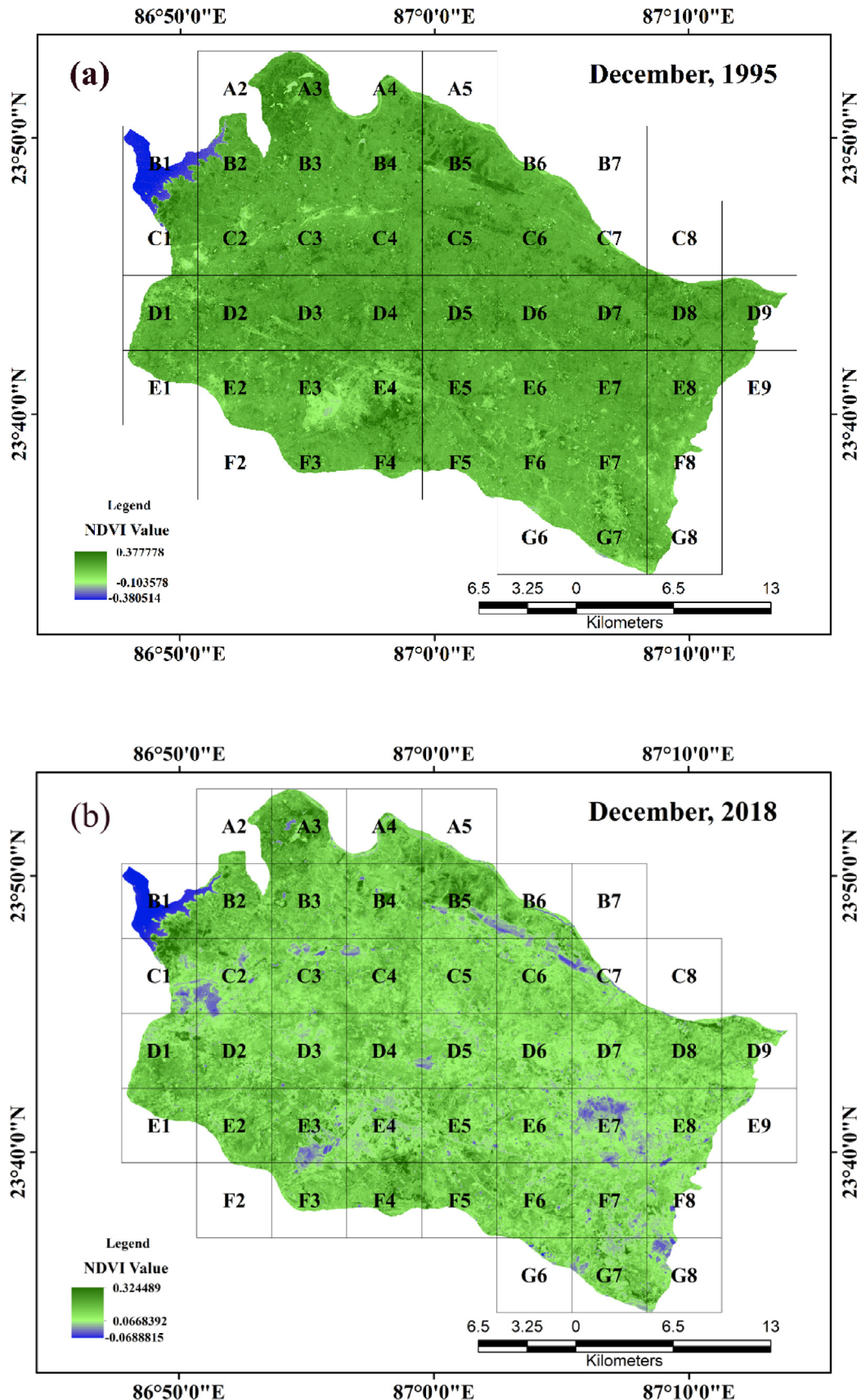
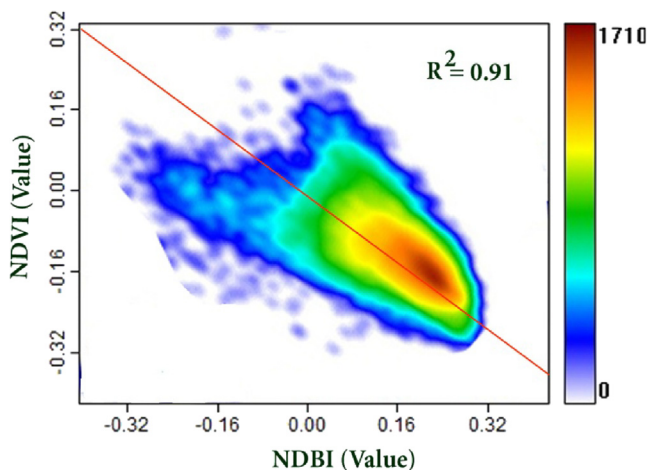


Fig. 15. (a) and (b) Spatial pattern of NDVI.



**Fig. 16.** Relation between NDBI and NDVI.

perature is increased in the grid of B5, B6, C7, C2 & C3, where coal mines are located. Again higher temperature shows in grid F3, F6, F7 where the industrial town Asansol and Raniganj are present and E7 and E8 which is characterized by brick kilns. So, for the awareness of our near future this prediction may open the eyes of the higher authorities and they may take precaution against the future rise of temperature. In this ground, this research may be fruitful for our next generation.

#### 4. Conclusion

This study attempted to find out the fact that the increasing trend of temperature over the land area has been recorded both during summer and winter season. This research also explores that temperature remains above 42 °C at coal mines, industrial patches, and built-up areas. The changing trend of ground surface temperature depicts that maximum and minimum temperature during the summer season has been increased about 0.15 °C and

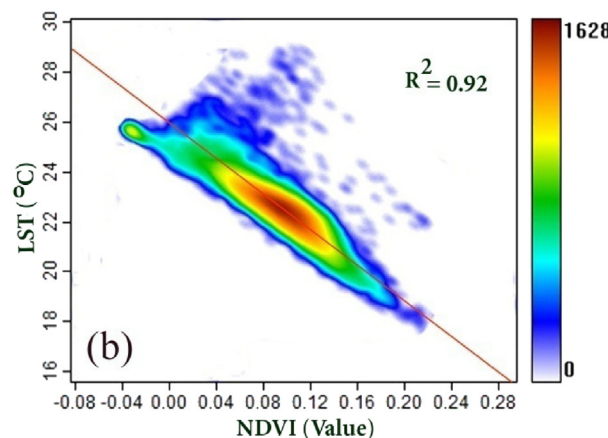
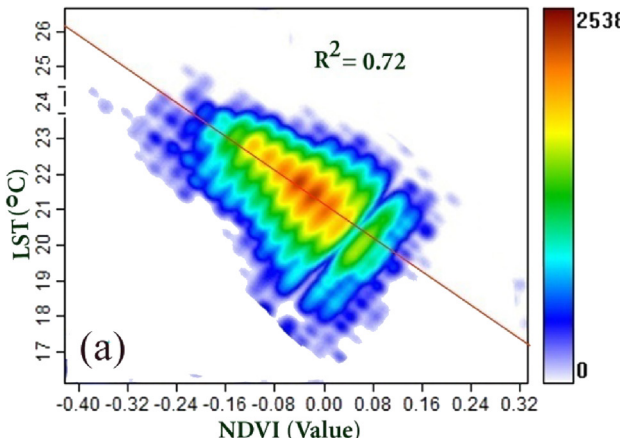
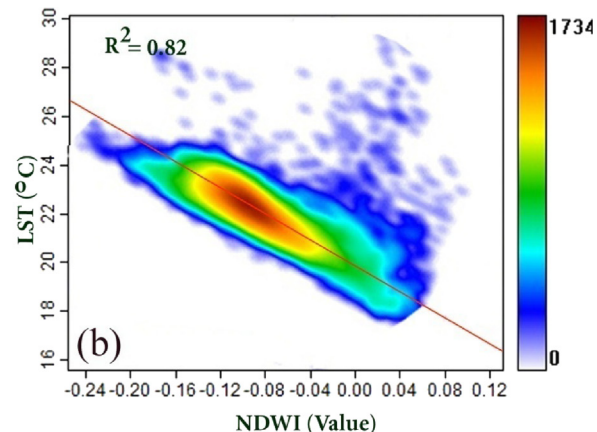
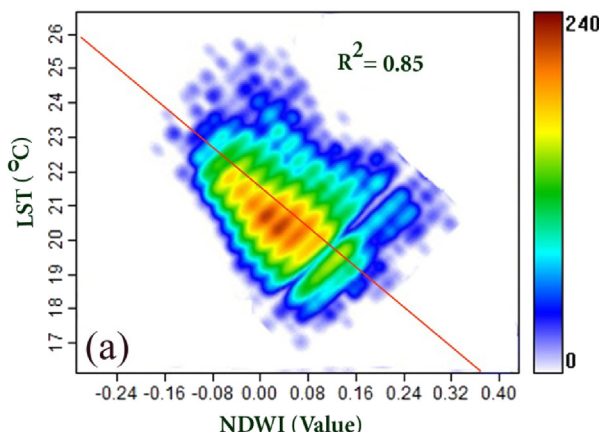


**Fig. 17.** (a) and (b) Relation between LST and NDVI of 1995(a) and 2018(b).

**Table 9**

Correlation matrix between LST and other spatial indices (1995).

	LST	NDVI	NDWI	NDBI
LST	1	-0.95	-0.92	0.93
NDVI	-0.95	1	0.88	-0.95
NDWI	-0.92	0.88	1	-0.89
NDBI	0.93	-0.95	-0.89	1

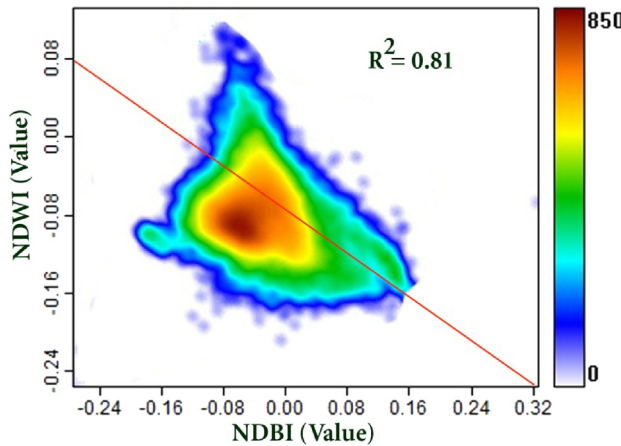


**Fig. 18.** (a) and (b) Relation between LST and NDWI of 1995(a) and 2018(b).

**Table 10**

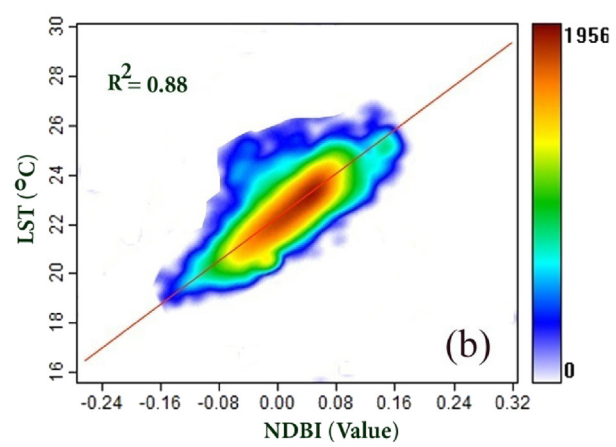
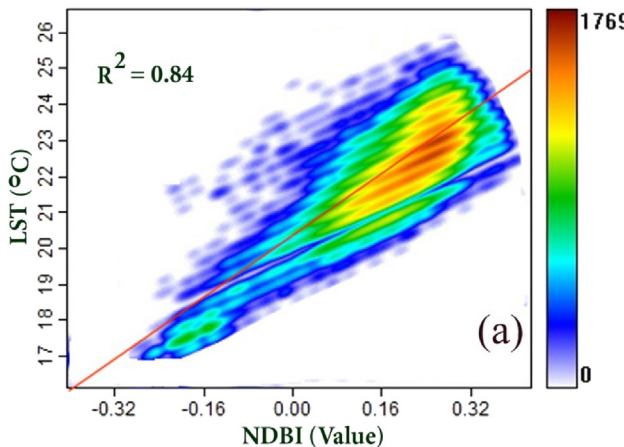
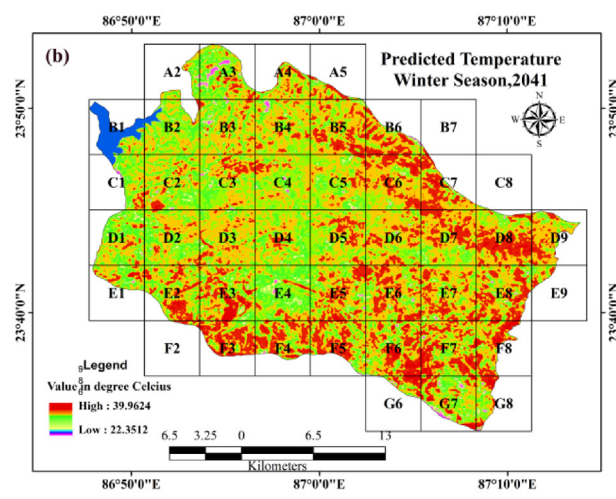
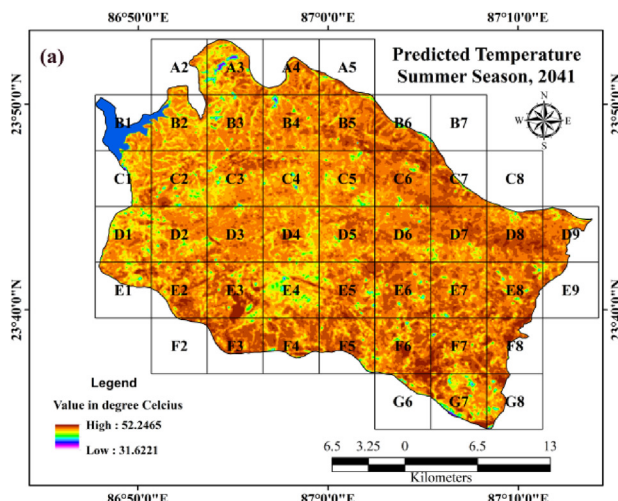
Correlation matrix between LST and other spatial indices (2018).

	LST	NDVI	NDWI	NDBI
LST	1	-0.84	-0.9	0.91
NDVI	-0.84	1	0.84	-0.9
NDWI	-0.9	0.84	1	-0.85
NDBI	0.93	-0.9	-0.85	1

**Fig. 19.** The relation between NDBI and NDWI.

0.011 °C per year respectively over 23 years. On the other hand, the maximum and minimum temperature during the winter season has also been increased at the rate of 0.19 °C and 0.05 °C per year respectively over the corresponding 23 years.

In this respect, a plan for Asansol subdivision: Land Use and Development Control Plan – 2025 has been taken into consideration. They emphasize the development of the local environment, enhance the quality of life and development of physical infrastructure. In the case of land use planning, they emphasize the development of the zonation of the residential and industrial areas. Moreover, the unused fallow land should be converted into vegetation land so that increasing surface temperature will be under control. In the urban areas, more vegetation should be planted and more parks should be constructed with dense vegetation like Chittaranjan. For the implementation of all these things, strict planning must be applied in this region. This may help to control further temperature increase.

**Fig. 20.** (a) and (b) Relation between LST and NDBI of 1995(a) and 2018(b).**Fig. 21.** (a) and (b) Predicted temperature of 2041 for both summer and winter Season.

## Declaration of Competing Interest

The authors declare that they have no known competing financial interests or personal relationships that could have appeared to influence the work reported in this paper.

## References

- Asgarian, A., Amiri, B., Sakieh, Y., 2014. Assessing the effect of green cover spatial patterns on urban land surface temperature using landscape metrics approach. *Urban Ecosyst.* 18, 209–222. <https://doi.org/10.1007/s11252-014-0387-7>.
- Bhattacharjee, S., Mitra, P., Ghosh, S.K., 2014. Spatial interpolation to predict missing attributes in GIS using semantic kriging. *IEEE Trans. Geosci. Remote Sens.* 52 (8), 4771–4780. <https://doi.org/10.1109/TGRS.2013.2284489>.
- Choudhury, D., Das, K., Das, A., 2019. Assessment of land use/land cover changes and its impact on variations of land surface temperature in Asansol-Durgapur Development Region, Egypt. *J. Remote Sens. Sp. Sci.* 22, 203–218. <https://doi.org/10.1016/j.ejrs.2018.05.004>.
- Cohen, J.A., 1960. Coefficient of agreement for nominal scales. *Educ. Psychol. Meas.* 20, 37–46.
- Das, N., Mukhopadhyay, S., 2018. Application of multi-criteria decision making technique for the assessment of groundwater potential zones: a study on Birbhum district, West Bengal, India. *Environ. Dev. Sustain.* doi: 10.1007/s10668-018-0227-7.
- Dissanayake, D., Morimoto, T., Ranagalage, M., Murayama, Y., 2019. Land-use/land-cover changes and their impact on surface urban heat islands: case study of Kandy City, Sri Lanka. *Climate* 99 (7), 2–20. <https://doi.org/10.3390/cli7080099>.
- Fahimi Nezhad, E., FallahGhalhari, G., Bayatani, F., 2019. Forecasting maximum seasonal temperature using artificial neural networks “Tehran case study”. *Asia-Pac. J. Atmos. Sci.* 55, 145–153. <https://doi.org/10.1007/s13143-018-0051-x>.
- Foody, G.M., 1992. On the compensation for chance agreement in image classification accuracy assessment. *Photogramm. Eng. Remote Sen.* 58, 1459–1460.
- Govind, N., Ramesh, H., 2019. The impact of spatiotemporal patterns of land use/land cover and land surface temperature on an urban cool island: a case study of Bengaluru. *Environ. Monit. Assess.* 191. <https://doi.org/10.1007/s10661-019-7440-1>.
- Hathout, S., 2002. The use of GIS for monitoring and predicting urban growth in East and West St Paul, Winnipeg, Manitoba, Canada. *J. Environ. Manage.* 66, 229–238. [https://doi.org/10.1016/s0301-4797\(02\)90596-7](https://doi.org/10.1016/s0301-4797(02)90596-7).
- Hirasawa, Y., Urakami, W., 2010. Study on specific heat of water adsorbed in zeolite using DSC. *Int. J. Thermophys.* 31, 2004–2009. <https://doi.org/10.1007/s10765-010-0841-6>.
- JokarArsanjani, J., Helbich, M., Kainz, W., DarvishiBoloorani, A., 2013. Integration of logistic regression, Markov chain and cellular automata models to simulate urban expansion. *Int. J. Appl. Earth Obs. Geoinform.* 21, 265–275. <https://doi.org/10.1016/j.jag.2011.12.014>.
- Jupp, D.L.B., 1989. The stability of global estimates from confusion matrices. *Int. J. Remote Sens.* 10, 1563–1569.
- Landis, J., Koch, G.G., 1977. The measurement of observer agreement for categorical data. *Biometrics* 33, 159–174.
- Mahato, S., Pal, S., 2018. Changing land surface temperature of a rural Ranchi tract river basin of India. *Remote Sens. Appl.: Soc. Environ.* 10, 209–223. <https://doi.org/10.1016/j.rsase.2018.04.005>.
- McFeeters, S.K., 1996. The use of normalized difference water index (NDWI) in the delineation of open water features. *Int. J. Remote Sens.* 17 (7), 1425–1432.
- Moldoveanu, G., Minea, A., 2019. Specific heat experimental tests of simple and hybrid oxide-water nanofluids: proposing new correlation. *J. Mol. Liq.* 279, 299–305. <https://doi.org/10.1016/j.molliq.2019.01.137>.
- Pal, S., Ziaul, S., 2017. Detection of land use/land cover change and land surface temperature in English Bazar urban centre. *J. Remote Sens. Sp. Sci.* 20, 125–145. <https://doi.org/10.1016/j.ejrs.2016.11.003>.
- Ranagalage, M., Dissanayake, D., Murayama, Y., Zhang, X., Estoque, R.C., Perera, E., Morimoto, T., 2018a. Quantifying Surface Urban Heat Island Formation in the World Heritage Tropical Mountain City of Sri Lanka. *Int. J. Geo. Infrm.* 7 (341), 2–18. <https://doi.org/10.3390/ijgi7090341>.
- Ranagalage, M., Estoque, R.C., Zhang, X., Murayama, Y., 2018b. Spatial changes of urban heat island formation in the Colombo District, Sri Lanka: implications for sustainability planning. *Sustainability* 10 (1367), 2–21. <https://doi.org/10.3390/su10051367>.
- Ranagalage, M., Murayama, Y., Dissanayake, D., 2019. The Impacts of Landscape Changes on Annual Mean.
- Ranagalage, M., Wang, R., Gunaratna, M.H.J.P., Dissanayake, D., Murayama, Y., Simwanda, M., 2019b. Spatial forecasting of the landscape in rapidly urbanizing hill stations of South Asia: a case study of Nuwara Eliya, Sri Lanka (1996–2037). *Remote Sens.* 1743 (11), 2–31. <https://doi.org/10.3390/rs11151743>.
- Rousta, I., Sarif, O., Gupta, R.V., Olafsson, H., Ranagalage, M., Murayama, Y., Zhang, H., Mushore, T.D., 2018. Spatiotemporal analysis of land use/land cover and its effects on surface urban heat island using Landsat data: a case study of metropolitan city Tehran (1988–2018). *Sustainability* 10 (4433), 2–25. <https://doi.org/10.3390/su10124433>.
- Saba, T., Rehman, A., AlGhamdi, J., 2017. Weather forecasting based on hybrid neural model. *Appl. Water Sci.* 7, 3869–3874. <https://doi.org/10.1007/s13201-017-0538-0>.
- San, T.H.H., Khin, M.M., 2016. River Flood Prediction Using Markov Model. In: Zin, T., Lin, J.W., Pan, J.S., Tin, P., Yokota, M., (Eds.), *Genetic and Evolutionary Computing. Advances in Intelligent Systems and Computing*, vol 387. Springer, Cham.
- Story, M., Congalton, R.G., 1986. Accuracy assessment: a user's perspective. *Photogramm. Eng. Remote Sens.* 52, 397–399.
- Tetteyey, M., Oduro, F., Adedia, D., Abaye, D., 2017. Markov chain analysis of the rainfall patterns of five geographical locations in the south eastern coast of Ghana. *Earth Perspectives* 4. <https://doi.org/10.1186/s40322-017-0042-6>.
- Townshend, J.R., Justice, C.O., 1986. Analysis of the dynamics of African vegetation using the normalized difference vegetation index. *Int. J. Remote Sens.* 7 (11), 1435–1445.
- Weng, Q., Lu, D., Schubring, J., 2004. Estimation of land surface temperature–vegetation abundance relationship for urban heat island studies. *Remote Sens. Environ.* 89, 467–483. <https://doi.org/10.1016/j.rse.2003.11.005>.
- Zha, Y., Gao, J., Ni, S., 2003. Use of normalized difference built-up index in automatically mapping urban areas from TM imagery. *Int. J. Remote Sens.* 24 (3), 583–594.
- Zhang, W., Huang, B., 2015. Land use optimization for a rapidly urbanizing city with regard to local climate change: Shenzhen as a case study. *J. Urban Plan. Dev.* 141 (1). Article ID 05014007.
- Zhou, Q., Robson, M., Pilesjo, P., 1998. On the ground estimation of vegetation cover in Australian rangelands. *Int. J. Remote Sens.* 9, 1815–1820.